

## Contact compliance effects in the frictional response of bioinspired fibrillar adhesives

Marco Piccardo, Antoine Chateaminois, Christian Fretigny, Nicola M. Pugno and Metin Sitti

*J. R. Soc. Interface* 2013 **10**, 20130182, published 3 April 2013

---

### References

[This article cites 28 articles, 6 of which can be accessed free](#)

<http://rsif.royalsocietypublishing.org/content/10/83/20130182.full.html#ref-list-1>

### Subject collections

Articles on similar topics can be found in the following collections

[biomimetics](#) (71 articles)

### Email alerting service

Receive free email alerts when new articles cite this article - sign up in the box at the top right-hand corner of the article or click [here](#)

[rsif.royalsocietypublishing.org](http://rsif.royalsocietypublishing.org)

## Research



**Cite this article:** Piccardo M, Chateauinois A, Fretigny C, Pugno NM, Sitti M. 2013 Contact compliance effects in the frictional response of bioinspired fibrillar adhesives. *J R Soc Interface* 10: 20130182.

<http://dx.doi.org/10.1098/rsif.2013.0182>

Received: 26 February 2013

Accepted: 11 March 2013

### Subject Areas:

biomimetics

### Keywords:

friction, shear failure, bioinspired adhesives, elastomer, gecko

### Author for correspondence:

Antoine Chateauinois

e-mail: [antoine.chateauinois@espci.fr](mailto:antoine.chateauinois@espci.fr)

# Contact compliance effects in the frictional response of bioinspired fibrillar adhesives

Marco Piccardo<sup>1,2</sup>, Antoine Chateauinois<sup>1</sup>, Christian Fretigny<sup>1</sup>, Nicola M. Pugno<sup>3</sup> and Metin Sitti<sup>4</sup>

<sup>1</sup>Laboratoire de Sciences et Ingénierie de la Matière Molle (SIMM), UMR CNRS 7615, Ecole Supérieure de Physique et Chimie Industrielles (ESPCI), Paris, France

<sup>2</sup>Département de Physique de l'Ecole Normale Supérieure (ENS), International Center for Fundamental Physics, 24 rue Lhomond, 75005 Paris, France

<sup>3</sup>Department of Civil, Environmental and Mechanical Engineering, University of Trento, via Mesiano, 77 38123 Trento, Italy

<sup>4</sup>Mechanical Engineering Department and Robotics Institute, Carnegie Mellon University, Pittsburgh, PA 15213-3890, USA

The shear failure and friction mechanisms of bioinspired adhesives consisting of elastomer arrays of microfibrils terminated by mushroom-shaped tips are investigated in contact with a rigid lens. In order to reveal the interplay between the vertical and lateral loading directions, experiments are carried out using a custom friction set-up in which normal stiffness can be made either high or low when compared with the stiffness of the contact between the fibrillar adhesive and the lens. Using *in situ* contact imaging, the shear failure of the adhesive is found to involve two successive mechanisms: (i) cavitation and peeling at the contact interface between the mushroom-shaped fibre tip endings and the lens; and (ii) side re-adhesion of the fibre's stem to the lens. The extent of these mechanisms and their implications regarding static friction forces is found to depend on the crosstalk between the normal and lateral loading directions that can result in contact instabilities associated with fibre buckling. In addition, the effects of the viscoelastic behaviour of the polyurethane material on the rate dependence of the shear response of the adhesive are accounted for.

## 1. Introduction

Thorough studies have shown that insects and geckos have evolved fibrillar hierarchical structures in order to improve climbing ability, which requires both locomotion and adhesion skills [1]. Over the past decade, these observations inspired the development of several bioinspired adhesives consisting of arrays of micro/nanofibres. As detailed in a recent review by Jagota & Hui [2], such fibrillar adhesives often show enhanced adhesive properties when compared with flat unstructured surfaces by virtue of mechanisms such as contact splitting or fibril energy losses. While the dependence of adhesive properties of fibrillar surfaces on parameters such as fibre shape and spacing, fibre orientation and elasticity are now relatively well understood and modelled, investigation of their frictional properties remains relatively scarce. When the synthetic fibrillar surfaces are made of stiff materials such as carbon nanotubes, much higher friction forces than flat surfaces of the same materials are often achieved [3–6]. However, such surfaces exhibit reduced adhesive properties owing to fibre stiffness and unevenness in fibre length. On the other hand, soft adhesive fibres arrays that are terminated either with a thin film or a spatula were shown to have considerably greater adhesion than that of flat surfaces of the same materials [7–9]. Moreover, these adhesive properties can be combined with several interesting frictional properties. As an example, it was shown that arrays of soft fibres connected by a terminal thin film [10–13] can exhibit high-static friction, as defined

from the peak in shear force in a friction experiment. In these experiments, static friction was found to be controlled by a crack-like contact instability associated with a release of the shear strain energy between the indenter and the sample. Accordingly, static friction enhancement was attributed to a crack-trapping mechanism related to the space fluctuations in the energy release rate which are induced by the fibre array. Other results were also reported by Varenberg & Gorb [14] and Kim *et al.* [15] in the case of fibrillar arrays with mushroom-shaped tip endings of similar shapes. Using polyvinylsiloxane (PVS)-patterned surfaces, Varenberg and Gorb found that static friction of the structured sample was always lower than the flat control. Conversely, Kim *et al.* observed a significant enhancement in static friction when compared with unstructured surfaces. However, the peak force associated with static friction was observed in both studies to involve the detachment of the terminal plates of the fibrils from the contacting glass surface. Once a mushroom-shaped fibre tip loses contact, the fibre bends and bears normal and lateral loads on its edge. As a result, the actual contact area is reduced. The observed decrease in the shear force at the static friction peak thus corresponds to a drop in the actual contact area as less and less fibre tips adhere to the glass surface. These observations thus support the fact that a high-static friction force mostly requires good adhesion of the fibre tips. As argued by Kumar & Hui [16] and Jagota & Hui [2], the contrasting results of Varenberg and Gorb as well as Kim *et al.* could result from the fact that the experiments are realized either at an imposed normal load [14] or at constant vertical displacement [15]. When a fibre is sheared, its buckling load can decrease significantly [10,17]. Under a constant normal load, fibres can thus easily buckle and could therefore more easily detach than under a constant vertical displacement. More generally, such a picture indicates that, under shear loading, the shear dependence of the vertical compliance of fibre arrays could introduce strong coupling between the normal and vertical loading direction which, in turn, may affect static and dynamic friction forces.

In this study, this issue is investigated by detailed shear experiments where the normal compliance of the set-up is varied in order to modulate the extent of coupling between the normal and lateral response of soft fibrillar arrays with mushroom-shaped endings. In §4, normal contact conditions are detailed with an emphasis on the onset of fibre buckling. In §5, the generic fibres' deformation mechanisms involved under shear are detailed. In addition to the previously reported stiction peak associated with detachment of the mushroom tip, a second stiction peak is identified that corresponds to a re-adhesion mechanism between the fibre stem and the contacting surface. The occurrence of these two mechanisms and their implications in the static friction force are further discussed from experiments where the vertical compliance of the device is varied. The rate dependence of the static friction force is also investigated and shown to involve some contribution of the bulk viscoelastic properties of the fibre material.

## 2. Elastomer microfibre array

A polyurethane (PU) elastomer microfibre array previously designed by Murphy *et al.* [18] is used for all experiments. As shown in figure 1, microfibres are terminated by

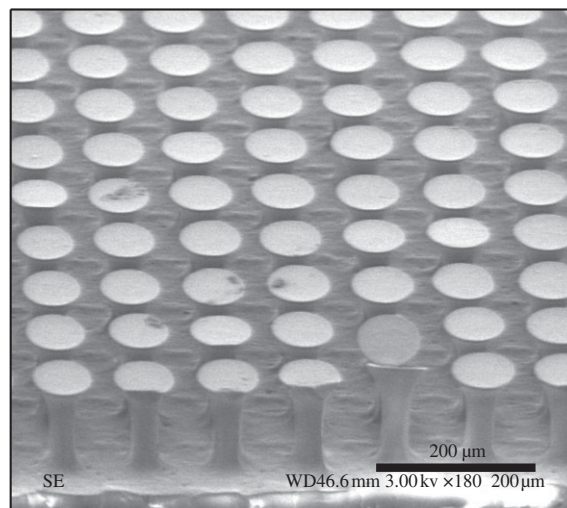


**Figure 1.** Scanning electron microscopy image of the microfibre array with mushroom-shaped endings.

mushroom-shaped tips. While mimicking the terminal shape of gecko's setae, this geometry strongly enhances adhesion by minimizing contact edge singularities [7,8,15,19]. Fibres are characterized by a length of 100  $\mu\text{m}$ , a tip radius of 45  $\mu\text{m}$  and a stem radius of 20  $\mu\text{m}$ . The thickness of the backing layer is about 40  $\mu\text{m}$ . Spacing between the edges of the mushroom-shaped tips of the fibres is 30  $\mu\text{m}$  in the orthogonal axis of the square lattice and 80  $\mu\text{m}$  in the diagonal direction. The Young modulus of PU material is measured using a thin (100  $\mu\text{m}$ ) film of the same material, and a contact method described elsewhere [20]. At 1 Hz, the storage and loss shear modulus are found to be 2.1 and 0.84 MPa, respectively.

## 3. Experimental set-up

Friction experiments are carried out using a sphere-on-flat contact configuration where a rigid spherical indenter (sapphire lens with a radius of curvature of 25 mm) is contacting the fibrillar array. Measurements are carried out using a custom micro-tribometer. A schematic of the set-up detailing the contact loading configuration in the normal direction is shown in figure 2. The lens indenter is fixed to a vertical translation stage (Microcontrole, UMR 8.25) by means of a cantilever with two arms. By changing the thickness and/or the material (stainless steel or brass) of the arms, the stiffness of the cantilever can be varied from a stiff ( $81.3 \times 10^3 \text{ N m}^{-1}$ ) to a compliant ( $1.6 \times 10^3 \text{ N m}^{-1}$ ) situation. In comparison, the normal contact stiffness achieved with the fibrillar array, and the lens ranges between  $3 \times 10^3$  and  $17 \times 10^3 \text{ N m}^{-1}$  depending on the contact conditions. In the following part of this paper, the set-up configuration using the rigid (resp. flexible) cantilevers will be denoted as the stiff (resp. compliant) set-up configurations. An optical fibre (Philtex, model D25) mounted on the vertical stage allows measurement of the deflections of the blades owing to the indentation process. A mirror is located on the cantilever tip that provides a reflecting surface for the displacement sensor. Then, knowing the stiffness of the cantilever, the applied normal load can be calculated from the measured deflection of the cantilever. A separate measurement of the indentation depth of the lens within the microfibre array is provided with a 0.1  $\mu\text{m}$  resolution by means of a non-contact

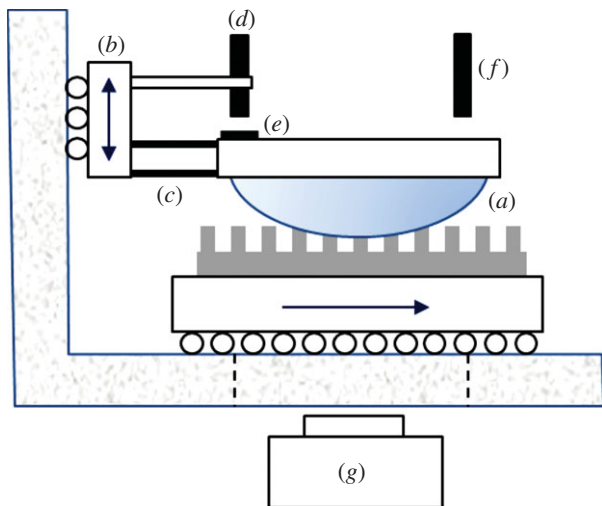


**Figure 2.** Schematic of the custom friction set-up detailing the normal contact loading configuration. A spherical indenter (*a*) is fixed to a vertical translation stage (*b*) by means of a cantilever with two flexible arms (*c*). By changing the thickness and/or the materials properties of the arms, it is possible to vary the stiffness of the device in the vertical direction. During the application of the normal contact loading, a measurement of the deflection of the cantilever by means of an optical fibre (*d*) and a reflecting surface (*e*) allows determination of the applied normal load. The indentation depth of the lens within the fibrillar adhesive is measured using an additional laser displacement transducer (*f*) fixed with respect to the instrument frame. During experiments, the fibrillar array is sheared at constant velocity using a motorized stage. A load cell (not shown in this figure for sake of clarity) measures the lateral load along an axis which is aligned with respect to the contact plane. Images of the contact region through the microfibre array are recorded with a zoom lens and a CMOS camera (*g*). (Online version in colour.)

laser displacement transducer (Keyence, LK-G187). The lens holder is fixed to the tip of the cantilever by means of a set of leaf springs loaded in tension along the vertical direction (not shown in figure 2 for sake of clarity). This arrangement provides a high (resp. low) stiffness in the normal (resp. lateral) directions while minimizing the crosstalk between these two directions (normal stiffness more than  $10^6 \text{ N m}^{-1}$ ; lateral stiffness less than  $10^4 \text{ N m}^{-1}$ ). During friction experiments, a lateral displacement at a constant velocity is applied to the fibrillar surface by means of a motorized translation stage (Physik Instrumente, M.403) while the lateral displacement is continuously monitored by means of an additional laser displacement transducer (Keyence, LKG-152). The lateral load is measured using a load cell transducer (Measurements Specialties, ELPF series, 50 N range) rigidly connected to the lens holder. Care has been taken to align the axis of the transducer with respect to the contact plane in order to avoid the application of a torque to the lens during frictional motion. A zoom lens mounted on a CMOS camera (PhotonFocus, MV1024E) records  $1024 \times 1024$  images of the contact region through the microfibre array at a frame rate of 10 Hz. Such bottom-view images are efficient in evaluating the collective behaviour of the array under friction but they cannot provide a detailed insight into single fibre mechanics. For that purpose, more resolved side-view observations of fibrils are carried out using another set-up described by Kim *et al.* [15] where the indenter and the sample can be oriented perpendicularly to the objective of the microscope. In addition, this device also allows for detailed top-view observations of the contact between individual fibre

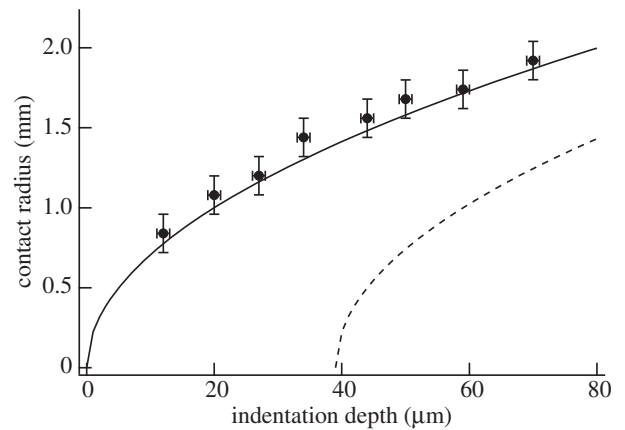


**Figure 3.** Measured contact radius as a function of the indentation depth. The solid line corresponds to the theoretical prediction of equation (4.1), the dotted line to the theoretical prediction for the radius of the buckled zone (equation (4.3)) using  $\Delta_c = 39 \mu\text{m}$  and  $R = 25 \text{ mm}$ .

tips and the lens. It was operated under imposed displacement conditions in the normal and lateral directions.

## 4. Normal contact

Figure 3 shows the change in the measured contact radius as a function of the indentation depth. Neglecting the deformation of the thin backing layer, the relationship between the contact radius  $a$  and the indentation depth  $\Delta$  can be estimated from purely geometrical considerations as

$$a = \sqrt{R^2 - (R - \Delta)^2} = \Delta \sqrt{\frac{2R}{\Delta} - 1}, \quad (4.1)$$

where  $R$  is the radius of curvature of the lens. As shown in figure 3, this prediction is in very good agreement with the experimental data. It is also of interest to estimate the critical indentation depth at the onset of fibre buckling. A single, perfectly cylindrical fibre under compression is expected to buckle at the Euler critical buckling load [21] defined as

$$P_c = \frac{\beta \pi^2 EI}{L^2}, \quad (4.2)$$

where  $E$  is the Young modulus,  $L$  is the fibre length and  $I$  is the moment of inertia and  $\beta = 4$  for clamped-clamped boundary conditions. As pointed out by several authors [2,22], this simple formula, while it is qualitatively correct, can only provide a broad estimate of the fibre's buckling load. Here, several deviations from the Euler theory are expected to occur due to the fact that the cross section is not uniform, the buckling strains are huge, so nonlinearities will matter, and the boundary conditions at the end of the fibril in contact with the backing layer are neither clamped in bending, nor fixed in the vertical direction. As a first-order approximation, the moment of inertia is taken as  $I = \pi a_s^4/4$ , where  $a_s$  is the stem radius. Estimating the axial stiffness from linear elasticity as  $k_a = (\pi a_s^2 E)/L$ , the critical displacement at the onset of buckling is calculated as  $\Delta_c = P_c/k_a = 39 \mu\text{m}$ . This theoretical prediction was compared with the value determined from experiments where the planar displacements of fibre cross sections during buckling are detected. A series of bottom-view images of the fibrillar array at different indentation depths are collected where the optics are focused at an intermediate height in between the

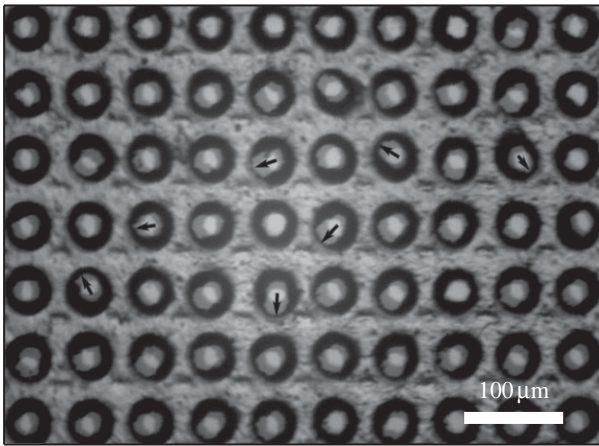


**Figure 4.** Superimposition of two bottom-view images of the fibrillar array taken at the centre of the contact and at two indentation depths,  $\Delta = 0$  and  $\Delta = 59 \mu\text{m}$ . Black circles correspond to the mushroom-shaped tips of the fibres, grey circles to the cross sections of the stems before and after indentation. The brighter spots correspond to the intersection of the shifted cross sections of buckled fibres with the corresponding cross sections in the unbuckled state. The bending directions of some of the buckled fibres are indicated by arrows (no correlation was detected).

top and bottom parts of the fibre extremities. Images are taken in the central part of the contact where buckling is expected to initiate. As shown in figure 4, superposition of successive images taken during indentation allows tracking of the lateral displacements of the stem cross sections. At low indentation depth, the stems are observed to enlarge without any shift of the centre, as expected from a purely compressive deformation of the fibrils. Above a critical indentation depth, cross sections of the stems are observed to shift randomly along the horizontal plane as a result of fibre bending above the Euler critical load. From these observations, the onset of buckling was found to occur between 30 and 40  $\mu\text{m}$  which is in qualitative agreement with the theoretical prediction ( $\Delta_c = 39 \mu\text{m}$ ).

According to equation (4.1), the radius,  $a_c$ , of the buckled portion of the contact area can be derived as

$$a_c = (\Delta - \Delta_c) \sqrt{\frac{2R}{\Delta - \Delta_c} - 1}, \quad (4.3)$$

which is shown as the dotted line in figure 3.

## 5. Shear deformation mechanisms

This section provides an overview of the fibres' deformation mechanisms under shear. For comparison purposes, the shear failure mechanisms of a smooth PU film confined between two rigid substrates are also briefly presented. Here, the main features of the shear response of the fibrillar array are illustrated in the case of an indentation depth of 50  $\mu\text{m}$  using the stiff device configuration. The corresponding lateral load/displacement curve is depicted in figure 5. When shear proceeds, two load peaks are clearly identified before steady-state friction is achieved. The magnitude of these two peaks is much greater (about five times) than the steady-state friction force achieved at large imposed displacement.

During normal preloading, an adhesive contact is achieved between the mushroom-shaped tips of the compressed fibres and the lens indenter. As a result, fibres bend

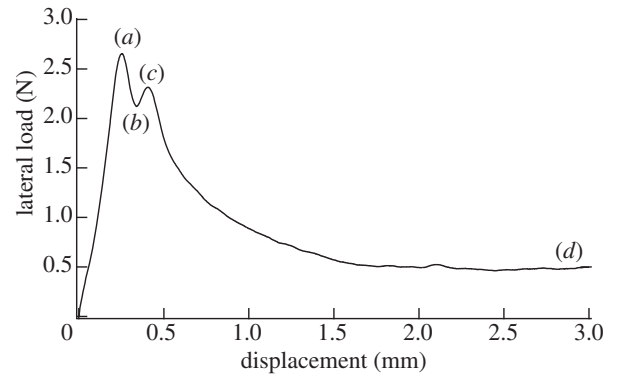


**Figure 5.** Lateral load as a function of imposed displacement during a shear loading using the stiff set-up configuration ( $\Delta = 50 \mu\text{m}$ , imposed velocity  $v = 100 \mu\text{m s}^{-1}$ ). (a) Cavitation, (b) peeling, (c) stem re-adhesion and (d) steady-state friction (see text for details).

and are subjected to an axial stretch when shearing proceeds. The lateral component of the corresponding stretching force results in the observed increase in lateral load up to the occurrence of a first load peak. The associated deformation mechanisms are detailed in figure 6*a* which shows a sequence of top-view images of the contact between a fibre tip and the lens for increasing imposed displacement close to the first load peak. A void is clearly seen to nucleate and grow at the contact interface according to a cavitation mechanism. Such a cavitation process is favoured by the mushroom geometry that tends to minimize stress concentration at the edge of the contact between the fibre tip and the lens. As a result, cavitation is favoured when compared with crack opening mechanisms at the periphery of the contact. When nucleated, voids grow nearly isotropically until they reach the edges of the tips. Then, debonding occurs between the tip and the lens according to a peeling mechanism schematized in figure 7*b*. This peeling process results in a crescent shape of the contact between the fibre tip and the lens, which is shown in the last image in figure 6*a*. Peeling of the mushroom-shaped tips allows for a relaxation of the fibre axial stretch and a corresponding reduction in the lateral force. The transition between cavitation and peeling mechanisms thus corresponds to the first load peak in figure 5.

As shown in figure 6*b*, mushroom-shaped tip peeling is associated with a re-adhesion mechanism between the stem of the fibres and the lens for the considered indentation depth. This re-adhesion mechanism allows for an additional stretch of the fibre which results in a re-increase in the lateral load. In figure 6*b*, the stretch of the stem can be tracked from the displacement of the mushroom root (R) with respect to the fibre/lens contact. At the same time, peeling of the tip still proceeds as indicated by the vanishing crescent shape of the contact between the mushroom-shaped tip and the lens. When the mushroom-shaped tip is completely peeled off, full sliding occurs between the lens, and the contacting part of the stem and the system is subjected to a transition to steady-state friction as schematized in figure 7*c,d*. Steady-state friction thus involves side contact between bent fibres and the lens. As a conclusion, the stiction of the fibrillar adhesive for the considered contact conditions is found to involve two successive mechanisms: (i) cavitation and peeling at the interface between the mushroom-shaped endings of the fibres and (ii) side re-adhesion of the fibres to the lens.

For comparison purposes, figure 8 depicts a stiction curve obtained using a smooth PU film adhering to a glass slide

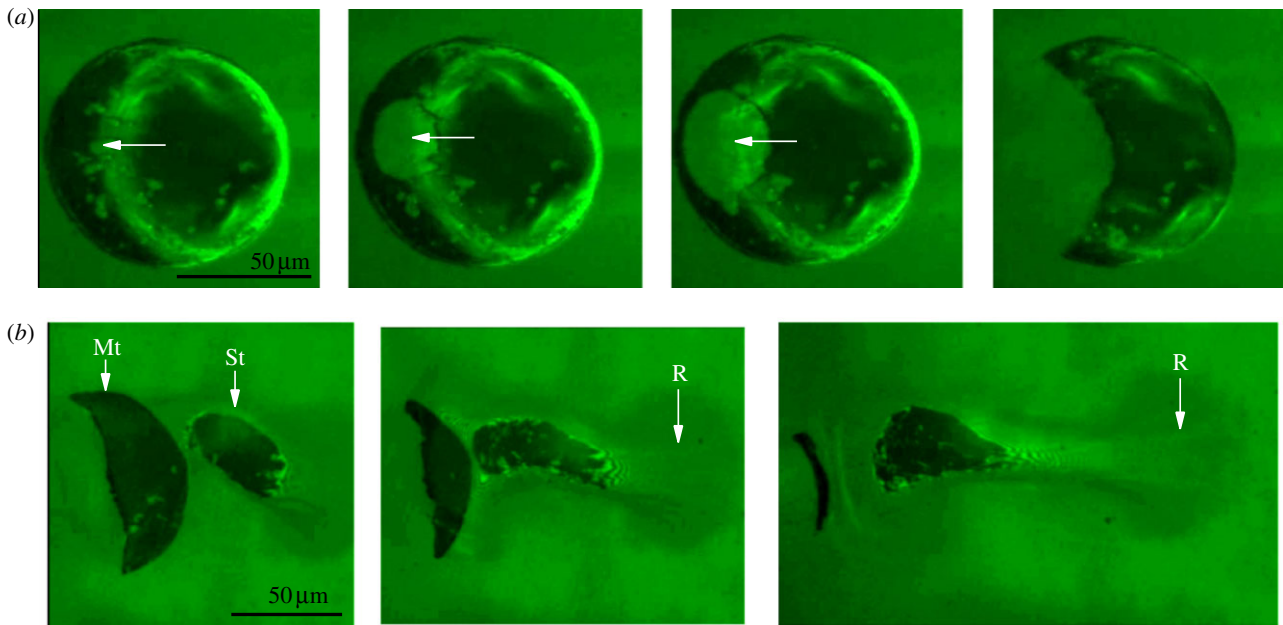


**Figure 6.** Sequence of top-view images showing deformation processes of a single fibre during shearing at imposed indentation depth (the fibrillar specimen is displaced from left to right with respect to the fixed lens). (a) Cavitation (as indicated by the white arrow) at the interface between the mushroom-shaped fibre tip and the lens. When the void reaches the contact edge, peeling of the mushroom-shaped fibre tip occurs which results in the crescent contact shape shown in the last image on the right. The occurrence of this peeling mechanism corresponds to the first load peak in figure 5. (b) Re-adhesion mechanism of the stem (St) inducing the second load peak in figure 5. The mushroom-shaped fibre tip (Mt) peels off while stretching of the stem can be observed from the displacement of the mushroom root (R) with respect to the contact zone. (Online version in colour.)

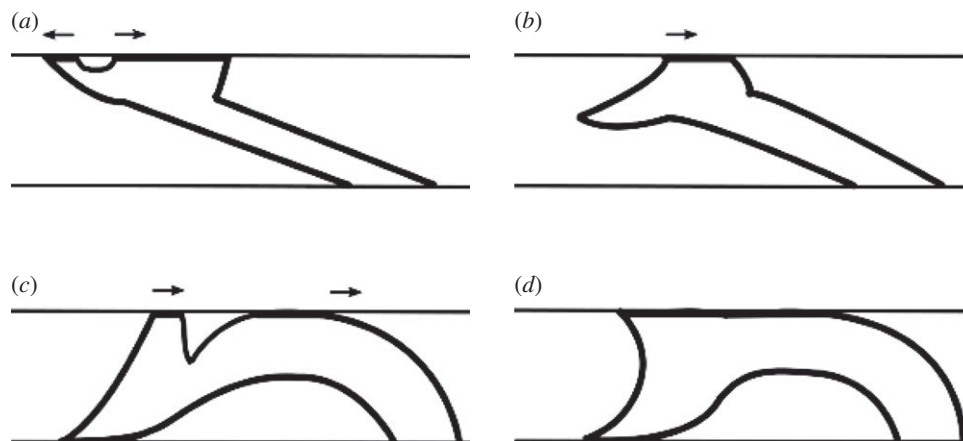


**Figure 7.** Schematic of the fibre deformation mechanisms under shear. (a) Void nucleation and growth at the interface between the mushroom-shaped fibre tip and the lens. (b) Peeling of the mushroom-shaped tip. (c) Re-adhesion of the stem. (d) Steady-state sliding. The fibrillar array is displaced from left to right with respect to the fixed top surface.

and the same indentation depth as for the fibre array. As a result of differences in the contact stiffness, the contact radius (1.3 mm) achieved with the flat PU film is smaller than that obtained with the fibrillar array (1.7 mm) for the same indentation depth. A sequence of bottom-view contact images is presented in figure 9. During the early shearing stages, the adhesive contact area becomes slightly elliptical (figure 9a) until peeling is induced at the trailing edge of the contact under the action of in plane tensile stresses. Peeling considerably reduces the contact area, which becomes semicircular shaped (figure 9b). Meanwhile, the adhesive contact sharply evolves into a sliding state. This sliding produces a displacement of the PU material towards the trailing edge of contact. Then, some part of the PU surface is observed to re-stick at the trailing edge of the contact

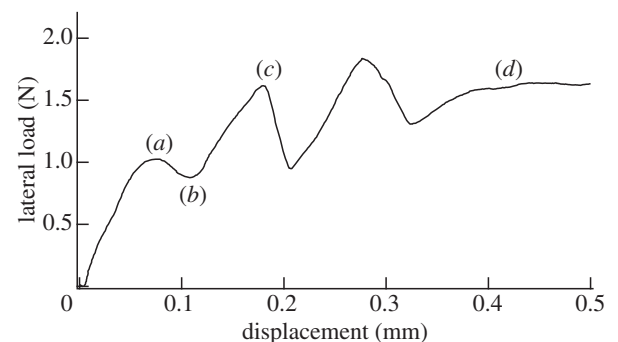


**Figure 8.** Lateral load as a function of imposed displacement for a smooth PU film approximately 100 μm in thickness (velocity: 100 μm s<sup>-1</sup>). The applied normal load is 560 mN (stiff set-up configuration).

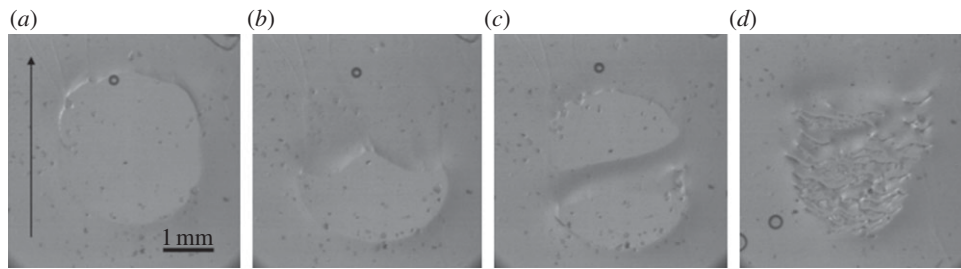


**Figure 9.** Sequence of bottom-view images showing the shear deformation mechanisms of the flat PU film (velocity:  $100 \mu\text{m s}^{-1}$ , preload: 560 mN corresponding to an indentation depth of  $50 \mu\text{m}$ , stiff set-up configuration). The PU specimen is moved from bottom to top with respect to the fixed lens as indicated by the arrow. (a–d) refer to various imposed displacements in figure 8.

(figure 9c). At this stage, the contact area is composed of two distinct adhesive regions separated by an air channel. Owing to this re-adhesion process, the lateral force further re-increases with the imposed displacement until full sliding is re-initiated (point (c) in figure 8). Similar re-adhesion mechanisms have already been reported by Barquins [23] within contacts between bulk rubber substrates and glass lenses and by Sosson *et al.* [24] in the case of thin layers of soft adhesives sheared between glass substrates. However, a detailed investigation of these contact instabilities is beyond the scope of this study. Here, it can just be noted that contact instabilities in the form of detachment waves (as shown in figure 9d) prevail as friction proceeds. In addition, it can be noted that the nominal shear stress corresponding to the first load peak (a) in figure 8 ( $0.18 \text{ MPa}$ ) is slightly lower than that corresponding to the first stiction peak of the fibrillar array ( $0.25 \text{ MPa}$ ).

## 6. Shear failure as a function of contact conditions

### 6.1. High normal stiffness case

Experimental stiction data presented in this section are obtained using the stiff set-up configuration at increasing applied indentation depths. As detailed below, some coupling arises between the normal and lateral loading directions that induce a change in the normal load during shearing. For the considered cantilever stiffness, the corresponding increase in indentation depth ranges from about  $1 \mu\text{m}$  for  $\Delta = 20$  to  $15 \mu\text{m}$  for  $\Delta = 70 \mu\text{m}$ . As indicated by the indentation data reported in figure 3, such a slight change in the indentation depth does not affect the contact radius by more than a few per cent. Another issue regarding the size of the contact during shearing is that, owing to the relative displacement of the adhesive with respect to the lens, some fibrils are engaging the sphere at the leading edge of the contact and some other fibrils are losing contact at the trailing edge of the contact. As an indication of the magnitude of this effect, it can be noted that the relative displacement of the sphere with respect to the adhesive specimen at the last stiction peak represents only between 10 per cent and 15 per cent of the contact diameter.

A series of static friction curves for fibres under varying imposed indentation depths is presented in figure 10. Indentation depths range from 20 to  $70 \mu\text{m}$ , including non-buckled and buckled states. For all the indentation depths under consideration, the fibrillar array exhibits a first cavitation peak that occurs at a constant imposed displacement of about  $240 \mu\text{m}$ . For the highest indentation depths (50, 60 and

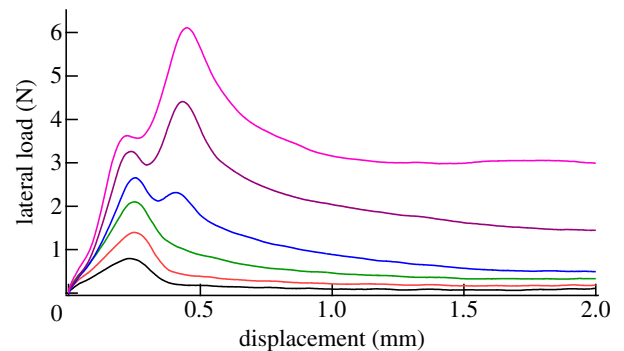


**Figure 10.** Lateral load as a function of imposed displacement for various indentation depths using the stiff set-up configuration (velocity:  $100 \mu\text{m s}^{-1}$ ). Indentation depth from bottom to top:  $20 \mu\text{m}$ ,  $30 \mu\text{m}$ ,  $40 \mu\text{m}$ ,  $50 \mu\text{m}$ ,  $60 \mu\text{m}$  and  $70 \mu\text{m}$ . (Online version in colour.)

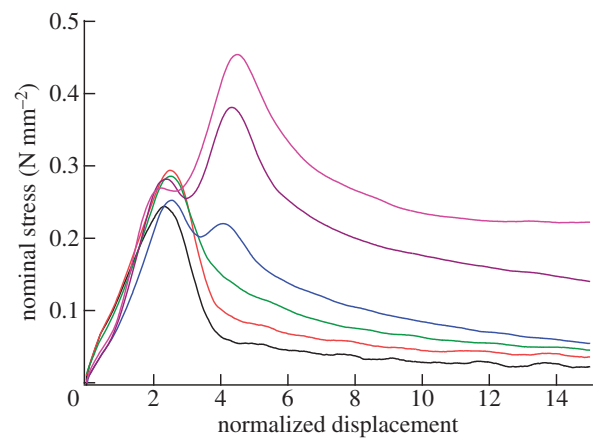


**Figure 11.** Normalized plot of lateral load as a function of imposed displacement using the stiff set-up configuration. The lateral load and imposed displacement have been normalized with respect to the apparent contact area and the fibres length, respectively. Indentation depth, from bottom to top:  $20 \mu\text{m}$ ,  $30 \mu\text{m}$ ,  $40 \mu\text{m}$ ,  $50 \mu\text{m}$ ,  $60 \mu\text{m}$  and  $70 \mu\text{m}$ . (Online version in colour.)

$70 \mu\text{m}$ ), the second load peak associated with stem adhesion is also observed at a displacement of about  $430 \mu\text{m}$ . The disappearance of the second load peak at the lowest indentation depths can be attributed to the fact that the fibres are not bent enough to allow for a contact between the stem and the lens for the considered gap between the surfaces. For all considered indentation depths, fibres exhibit a stable kinetic friction force which is much smaller than the load peak.

In figure 11, stiction curves are presented in a non-dimensional form where the lateral load has been divided by the apparent contact area, and the displacement has been

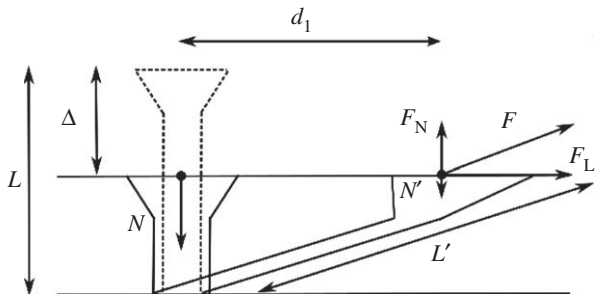


**Figure 12.** Schematic of fibre deformation under shear in the limit of a constant indentation depth. The displacement associated with the first peak is labelled as  $d_1$ . The preload,  $N$ , corresponds to a compression equal to  $\Delta$ . During shearing, fibre bending induces a decrease in normal stiffness. The normal load,  $N'$ , is thus decreasing. Meanwhile, owing to adhesion of the fibre tip to the lens, a tensile stretching  $F$  acts on the fibre: its lateral component  $F_L$  produces a lateral load, whereas the normal component  $F_N$  applies a vertical traction to the lens.

normalized with respect to the length of the fibres. This plot shows that the first peak during stiction corresponds to a nominal shear stress which is approximately constant when the indentation depth is varied. In other words, the magnitude of the first peak load is proportional to the number of fibrils engaging the sphere. It also turns out that the load peak associated with cavitation and peeling of the mushroom-shaped tip is dictated by the existence of critical stretch load or elongation ratio of the individual fibres. As schematized in figure 12, this critical stretch ratio,  $\lambda_L$ , can be deduced from purely geometrical consideration as

$$\lambda_L = \frac{L'}{L} = \frac{\sqrt{(L - \Delta)^2 + (d_1(\Delta))^2}}{L}, \quad (6.1)$$

where  $d_1(\Delta)$  is the value of the imposed lateral displacement at the first load peak. As  $(L - \Delta)^2 \ll d_1(\Delta)^2$  and  $d_1(\Delta)$  is weakly dependent on the indentation depth, a nearly constant value of  $\lambda_L = 2.5 \pm 0.2$  is calculated using equation (6.1) and the experimental values of  $d_1$ . The normalized plot also shows that the second load peak is no longer proportional to the numbers of fibres engaging the sphere and that some changes in the re-adhesion mechanisms must be considered. As suggested by the side-view observations reported in figure 13, a potential explanation for the increased nominal shear stress at high indentation depth would be that the size of each individual side contact between the stem and the lens increases with the indentation depth owing to enhanced fibre bending.

The measured changes in the normal load during the shear failure experiments are shown in figure 14. During shearing, a load reduction is systematically observed which results in a switch from positive (compression) to negative (tensile) normal load at the lowest indentation depths ( $\Delta \leq 40 \mu\text{m}$ ). Such a coupling between normal and lateral forces can be accounted for by the shear dependence of the normal compliance of the fibre array. As shearing occurs, fibres bend inducing a reduction in their normal stiffness. As a result, the normal load ( $N'$ ) applied under a nearly constant vertical displacement condition (figure 12) is decreasing. At the same time, fibres are subjected to a tensile stretch  $F$  owing to adhesion. The lateral component of this force  $F_L$  corresponds to the measured lateral load, whereas the normal component  $F_N$  applies a traction to the fibre. At low indentation depth, the change in the sign of the normal load indicates a transition from compression ( $N >$

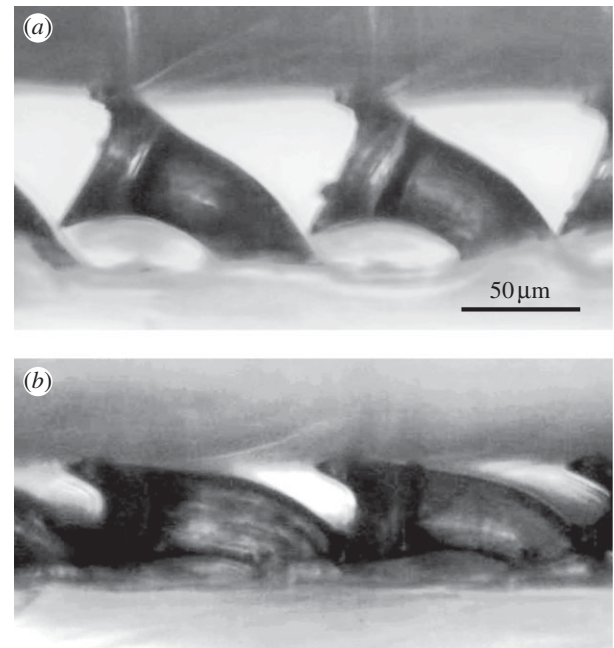


**Figure 13.** Side view of fibres during steady-state friction at (a) low and (b) high values of the indentation depth showing side contact between the fibres and the lens.

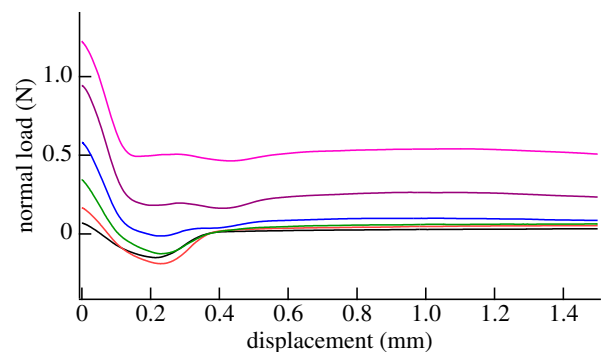


**Figure 14.** Normal load as a function of the imposed displacement using the stiff set-up configuration and different indentation depths (velocity:  $100 \mu\text{m s}^{-1}$ ). Indentation depth, from bottom to top:  $20 \mu\text{m}$ ,  $30 \mu\text{m}$ ,  $40 \mu\text{m}$ ,  $50 \mu\text{m}$ ,  $60 \mu\text{m}$  and  $70 \mu\text{m}$ . At low indentation depths ( $20$ ,  $30$  and  $40 \mu\text{m}$ ), a switch from compression to traction is seen to occur during the initial shearing stages. (Online version in colour.)

0) to traction ( $N' - F_N < 0$ ). Such a behaviour has been predicted theoretically by Kumar *et al.* [16] for a clamped fibre subjected to imposed normal and shear displacement.

Under steady-state sliding, the normal load corresponding to these indentation depths vanishes, which indicates that the vertical stiffness of the bent fibres is very low. Nevertheless, some finite friction force is still measured as a result of adhesive forces between fibres tips and the lens. It can also be observed that the second lateral load peak only occurs when the normal load at  $d_1$  is positive which means that the re-adhesion mechanism requires a net compressive normal load acting on the fibres.

Additional stiction experiments are also carried out under the same contact conditions with a PU flat control sample. A series of preloads comparable to those applied during fibres experiments are selected. Results are presented in figure 15. The flat film sample shows the frictional instabilities detailed earlier at all the considered contact conditions.

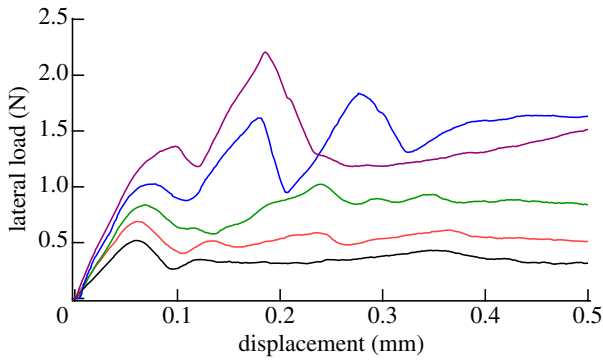


**Figure 15.** Lateral load as a function of imposed displacement for the flat PU film under various preloads (stiff set-up configuration, velocity:  $100 \mu\text{m s}^{-1}$ ). Preloads, from bottom to top: 85 mN, 200 mN, 325 mN, 560 mN and 925 mN. (Online version in colour.)

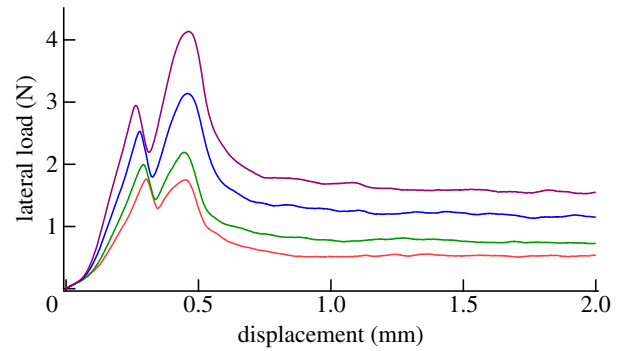


**Figure 16.** Lateral load as a function of imposed displacement using the compliant set-up configuration at different preloads. Preloads, from bottom to top: 70 mN, 120 mN, 210 mN and 350 mN. (Online version in colour.)

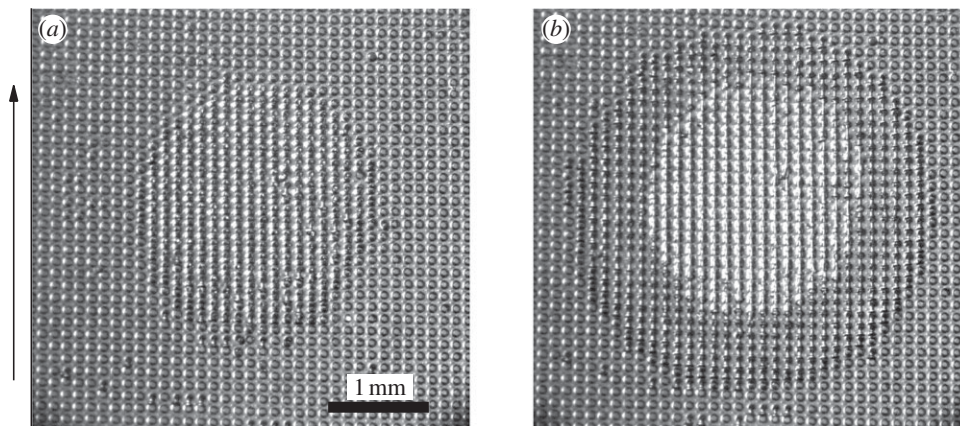


**Figure 17.** Bottom-view images of the contact sheared using the compliant set-up configuration (imposed preload: 120 mN). (a) Image acquired at an imposed lateral displacement of  $50 \mu\text{m}$ , i.e. at the onset of shearing. (b) Image taken for a displacement close to the first load peak. The brighter area in the right image contains fibres brought in contact during preload with mushroom-shaped fibre tips still adhering to the lens. The external darker annulus corresponds to fibres that went into side contact as a consequence of the increased indentation depth associated with contact instability. The arrow indicates the sliding direction.

In contrast to fibre array behaviour, the average kinetic friction force is in the order of magnitude of the stiction load.

## 6.2. Low normal stiffness case

In this section, we present results of experiments carried out using the compliant set-up configuration. This configuration allows for potential large variations in the indentation depth and limited changes in the normal load (typically  $\Delta N \leq 50 \text{ mN}$ ) when shear is applied. Because  $\Delta N$  is smaller than the applied preloads, experiments can be considered as carried out under a nearly constant normal load condition. Load–displacement curves are presented in figure 16. From contact observations, fibre deformation mechanisms were found to remain qualitatively unchanged when compared with the stiff set-up configuration. As opposed to the stiff set-up configuration, the second stiction peak occurs at all considered preloads. This can be explained by observing that the normal load remains always positive with this set-up configuration thus allowing for the re-adhesion mechanism between the fibres stems and the lens.

One of the main features of static friction process with the low stiffness configuration is the increase in contact area as shear proceeds. In figure 17, two bottom-view images are presented, showing the contact area at a low shear displacement (figure 17a) and when the first lateral load peak occurs (figure 17b). An increase in contact area is clearly visible in figure 17b where the inner, brighter, disc corresponds to

fibres initially brought into contact during preload with mushroom-shaped tip adhering to the lens, whereas the darker annulus contains bent fibres that went in side contact as shearing proceeded. As shown in figure 18, this enlargement of the contact area is correlated with an increase in indentation depth with shear displacement. As the normal stiffness of fibres decreases during shearing while the highly compliant device maintains a nearly constant normal contact load (within less than 50 mN), contact instability is induced which corresponds to a sharp increase in the indentation depth. In figure 18, the contact instability is seen to occur for a lateral displacement less than the fibre length ( $100 \mu\text{m}$ ) and lower than the imposed lateral displacement at the first peak force. From equation (4.1), it can be predicted that the increase in contact radius associated with the variation in indentation depth should be in the form of

$$b(\Delta') = b(\Delta_0) \left[ \frac{\Delta'}{\Delta_0} \sqrt{\frac{(2R - \Delta')\Delta_0}{(2R - \Delta_0)\Delta'}} \right], \quad (6.2)$$

where  $\Delta_0$  is the indentation depth associated with the imposed preload and  $\Delta'$  corresponds to the indentation depth at the first load peak. Observing that  $2R \gg \Delta_0, \Delta'$ , equation (6.2) simplifies as

$$b(\Delta') \simeq b(\Delta_0) \sqrt{\frac{\Delta'}{\Delta_0}} - 1. \quad (6.3)$$

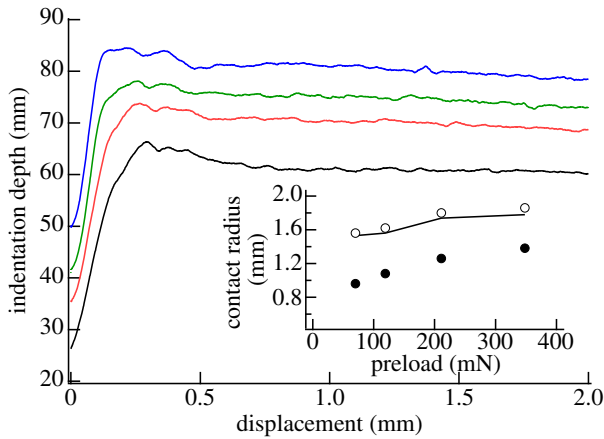


**Figure 18.** Changes in the indentation depth as a function of lateral displacement during shear experiments carried out at different preloads and using the compliant set-up configuration (velocity:  $100 \mu\text{m s}^{-1}$ ). Preloads, from bottom to top: 70 mN, 120 mN, 210 mN and 350 mN. The occurrence of a contact instability is indicated by the sharp increase in indentation depth at low imposed lateral displacement. Inset: contact radius (filled circles) before and (open circles) after the occurrence of the contact instability. Solid line denotes theoretical prediction of equation (6.3). (Online version in colour.)

As shown in the inset in figure 18, this theoretical prediction is in close agreement with the experimental data showing that the contact radius increases from 35 per cent to 63 per cent when the applied preload is decreased from 350 to 70 mN.

Despite this increase in contact radius, the nominal shear stress associated with the first stiction peak (between 0.23 and 0.27 MPa) is also relatively independent of the preload, thus indicating that the increase in peak load is due primarily to additional stalks in contact. This is no longer true for the second load peak (the associated nominal shear stress increases from 0.23 to 0.38 MPa when the preload increases from 70 to 350 mN), probably for the same reason (enhanced side contacts) as for the stiff set-up configuration.

## 7. Rate dependence

The velocity dependence of stiction has been investigated using the high stiffness set-up configuration. Experiments are carried out in a non-buckled state ( $\Delta = 30 \mu\text{m}$ ) and at shear velocities varying over about two decades. As shown in figure 19, the load peak associated with cavitation and peeling of the mushroom-shaped tips is clearly shifted to higher displacements and loads when the velocity is increased. As discussed in a recent adhesion study by Abusomwan & Sitti [25] using the same kind of PU fibrillar adhesive, this effect involves some contribution of the rate dependent work of adhesion. In addition, the increased slope of the load/displacement curves before the load peak also suggests a potential contribution of the viscoelastic tensile response of the fibres. An estimate of the time-dependent viscoelastic modulus of the fibres in this regime can be obtained from the measured load/displacement curves using the method derived by Basire & Fretigny [26]. Assuming a linear, causal and stationary response of the viscoelastic system

$$F_L \propto \int_0^t E(t-t') \dot{x}(t') dt', \quad (7.1)$$

where  $F_L$  is the lateral load response of the system,  $\dot{x} = v$  is the imposed shear velocity, and  $t$  and  $t'$  are time variables. Writing

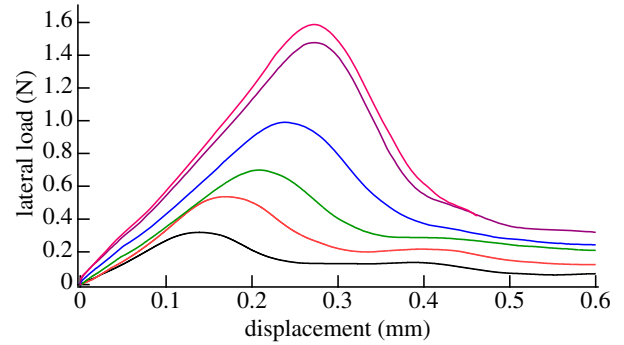


**Figure 19.** Lateral load as a function of the imposed displacement for varying imposed velocities. From bottom to top:  $3 \mu\text{m s}^{-1}$ ,  $10 \mu\text{m s}^{-1}$ ,  $30 \mu\text{m s}^{-1}$ ,  $100 \mu\text{m s}^{-1}$ ,  $300 \mu\text{m s}^{-1}$ ,  $500 \mu\text{m s}^{-1}$  (indentation depth:  $30 \mu\text{m}$ , stiff set-up configuration). (Online version in colour.)

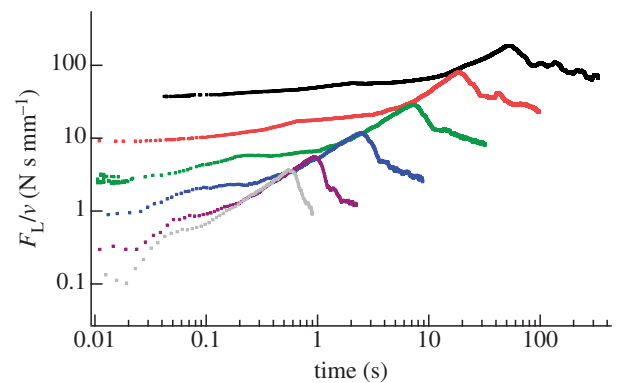


**Figure 20.** Log–log plot of the reduced lateral load,  $F_L/v$ , as a function of time for various driving velocities (indentation depth:  $30 \mu\text{m}$ , stiff set-up configuration). Same data as in figure 19. (Online version in colour.)

$u = t - t'$ , equation (7.1) can be expressed as

$$\frac{F_L}{v} \propto \int_0^t E(u) du. \quad (7.2)$$

In order to obtain the relaxation function, we differentiate equation (7.2)

$$\frac{d}{dt} \frac{F_L}{v} \propto E(t). \quad (7.3)$$

The time dependence of the viscoelastic modulus can thus be estimated from the experimental  $F_L/v$  ratio at different imposed velocities which is shown in figure 20.

The curves extend in the prolongation of each other up to the stiction peak and present a significant overlap. There is thus some indication that within a restricted domain located below the load peak, the lateral load is proportional to imposed velocity. At the small times, all the reduced load curves ( $F_L/v$ ) show a plateau region the magnitude of which is approximately proportional to the imposed velocity, i.e. the lateral load,  $F_L$ , is rate independent. Independent of the driving velocity, these plateau regions have a critical displacement in the order of  $30\text{--}40 \mu\text{m}$ , i.e. close to one diameter of the fibres. In this low displacement domain, deformation of the fibres is likely to predominantly involve bending rather than stretching. In other words, the reduced  $F_L(t)$  curves start to overlap when stretching becomes the dominant deformation mechanism. Within the overlap region, a power law fit of the experimental data provides  $F_L/v \propto t^{0.73}$ . From equation (7.3),  $E(t) \propto t^{-0.27}$ .

The time dependence of the viscoelastic modulus obtained with the fibrillar array can be compared with that of the bulk PU material. For that purpose, the viscoelastic shear modulus of the smooth PU film was measured using a contact method described fully elsewhere [20]. The principle of the measurement is to apply a very low amplitude oscillating shear deformation to the PU film confined between a flat glass substrate and glass lens. From a measurement of the in-phase and out-of-phase component of the lateral load response, the storage ( $G'$ ) and dissipative ( $G''$ ) components of the viscoelastic shear modulus ( $G^* = G' + iG''$ ) can be determined as a function of frequency. Then, the time-dependent shear modulus,  $G(t)$ , can be related to this complex modulus using the method of Ninomiya & Ferry [27]

$$G(t) = G'(\omega) - 0.40G''(0.40\omega) + 0.014G''(10\omega)|_{\omega=1/\tau}, \quad (7.4)$$

where  $G'$  is to be determined at  $\omega = 1/t$  and  $G''$  at two other frequencies. For the considered rubbery PU,  $G' < G''$  ( $\tan\delta \approx 0.4$  at 1 Hz) and as a first approximation equation (7.4) reduces to

$$G(t) \simeq G' \left( \frac{1}{t} \right). \quad (7.5)$$

The measured frequency dependence of the storage modulus at room temperature and between 0.3 and 5 Hz was found to obey a power law dependence,  $G' \propto f^{0.25}$ . According to equation (7.5), the related time dependence of the shear modulus should be  $G(t) \propto 1/f^{0.25} \propto t^{-0.25}$  which is very close to the time dependence obtained from shear experiments with the fibrillar adhesive. It can therefore be concluded that the linear viscoelastic behaviour of the fibrillar array reflects the viscoelastic properties of bulk PU.

## 8. Discussion

The shear failure mechanisms of the investigated fibrillar adhesive are observed to involve two successive mechanisms: (i) a rate-dependent cavitation and peeling process between the mushroom-shaped end of the fibres and the smooth surface of the lens and (ii) a re-adhesion mechanisms between the fibre stem and the lens that results in enhanced static friction forces. Before the occurrence of cavitation, it also emerged that the load response of the sheared fibrillar adhesive is dependent on the viscoelastic response of the stretched fibres adhering to the lens. Similar rate-dependent effects on friction were previously reported by Gravish *et al.* [28] for synthetic gecko setae. They were however much more limited, probably due to the fact that the used silicone elastomer was less viscoelastic than the PU material of this study. The viscoelastic properties of the PU fibres can be used to enhance adhesion and friction of these structures by increasing their strain rate during unloading or shearing as an additional control or design parameter for potential applications. For example, for a controlled pick-and-place manipulation or transfer printing application of elastomer microfibre adhesives as in the case of [29,30], a high retraction speed can be used to increase the adhesion of the fibres when picking a part while a very slow retraction speed during releasing the part would decrease the adhesion and facilitate the release.

The magnitude of the static friction force is clearly dependent on the normal compliance of the device. As shown in figure 21, the maximum shear forces achieved with the

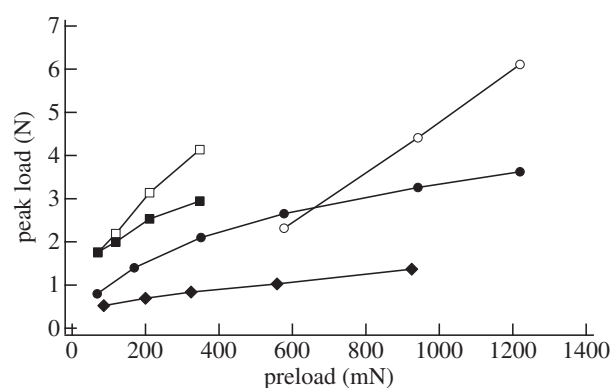


**Figure 21.** Maximum shear force at as a function of preload for the fibrillar adhesive and the unstructured PU film. Diamond, flat PU sample; circle, fibrillar array, stiff set-up configuration; square, fibrillar array, compliant set-up configuration. Filled and open symbols correspond to the first load peak (cavitation and peeling of the mushroom-shaped fibre tips) and to the second load peak (re-adhesion mechanism between the stems and the lens), respectively.

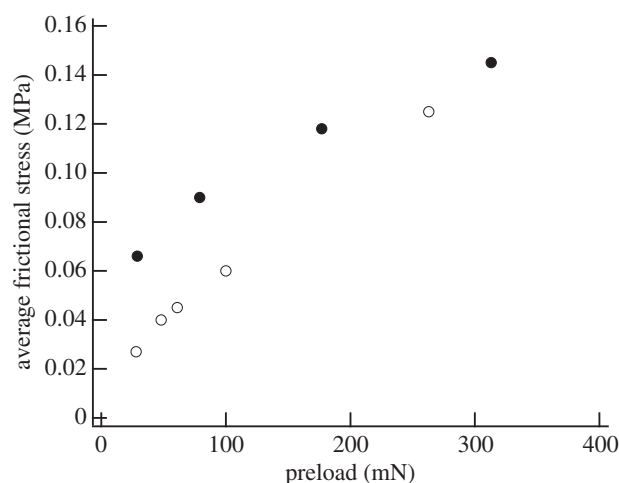


**Figure 22.** Average nominal frictional stress as a function of the applied preload. The frictional shear stress is calculated from the ratio of the friction force to the measured apparent contact area during steady-state friction. Filled circles, compliant set-up configuration; open circles, stiff set-up configuration.

compliant set-up are systematically higher than that obtained with the stiff configuration. This difference can be accounted for by the coupling between the normal and vertical direction which arises from the shear-dependent normal compliance of the fibre array. It is especially observed that the reduction in the normal compliance of the fibrillar adhesive at the onset of shear can result in a contact instability driven by the buckling of the fibres. When the normal compliance of the device is low enough, the main effect of this buckling instability is to induce an increase in the actual contact area that can account for the increased static friction peak. Another effect of the normal compliance of the device is also to modulate the extent of side contacts associated with the second load peak: for a given applied normal load, the actual contact area associated with side contact is obviously increasing when the vertical compliance of the device is high. When compared with a flat, unstructured surface, the fibrillar adhesive presents systematically higher static friction forces whatever the normal compliance. Interestingly, smooth steady-state friction is achieved with the fibrillar adhesives instead of stick-slip behaviour for the unstructured surface.

The coupling between normal and lateral loading directions also has some implications during steady-state friction. As shown in figure 22, the average frictional shear stress (as defined from the ratio of the steady-state friction force to the apparent contact area) is higher for the compliant configuration than for the stiff configuration, at least at low preloads. A compliant system will effectively enhance the individual contact areas between the fibres stems and the lens as fibre bending is promoted. This effect saturates at high preloads when the bent fibres stems are contacting both the lens and the backing layer of the fibrillar array.

From a biological or robotic perspective, the observed coupling between normal and vertical directions could allow for additional control of the shear failure and frictional properties of the adhesive through the modulation of the

vertical compliance of the adhesive systems. Understanding the static and dynamic friction mechanisms is crucial to the optimal design of these mushroom-shaped elastomer fibrillar structures for enhanced or controlled friction applications. Therefore, the results in this paper will be used as a guide for future work to optimize the fibre modulus, tip size, tip wedge angle, stem diameter, aspect ratio and spacing to maximize or minimize the fibre array's dynamic or static friction performance.

This work was supported by the National Research Agency (ANR) within the framework of the DYNALO project (no. NT09 499845). M.S. was supported by the NSF CMMI-1130520 project. The authors thank Uyiosa Abumsonwan for his help in the realization of the side-view experiments.

## References

- Arzt E, Gorb S, Spolenak R. 2003 From micro to nano contacts in biological attachment devices. *Proc. Natl Acad. Sci. USA* **100**, 10 603–10 606. (doi:10.1073/pnas.1534701100)
- Jagota A, Hui C-Y. 2011 Adhesion, friction, and compliance of bio-mimetic and bio-inspired structured interfaces. *Mater. Sci. Eng. Rep.* **72**, 253–292. (doi:10.1016/j.mser.2011.08.001)
- Aksak B, Murphy M, Sitti M. 2007 Adhesion of biologically inspired vertical and angled polymer microfiber arrays. *Langmuir* **23**, 3322–3332. (doi:10.1021/la062697t)
- Maeno Y, Nakayama Y. 2009 Geckolike high shear strength by carbon nanotube fiber adhesives. *Appl. Phys. Lett.* **94**, 012103. (doi:10.1063/1.3050450)
- Majidi C *et al.* 2006 High friction from a stiff polymer using microfiber arrays. *Phys. Rev. Lett.* **97**, 076103. (doi:10.1103/PhysRevLett.97.076103)
- Schubert B, Majidi C, Groff R, Baek S, Bush B, Maboudian R, Fearing R. 2007 Towards friction and adhesion from high modulus microfiber arrays. *J. Adhes. Sci. Technol.* **21**, 1297–1315. (doi:10.1163/156856107782328344)
- del Campo A, Greiner C, Arzt E. 2007 Contact shape controls adhesion of bioinspired fibrillar surfaces. *Langmuir* **23**, 10 235–10 243. (doi:10.1021/la7010502)
- Gorb S, Varenberg M, Peressadko A, Tuma J. 2007 Biomimetic mushroom-shaped fibrillar adhesive microstructure. *J. R. Soc. Interface* **4**, 271–275. (doi:10.1098/rsif.2006.0164)
- Kim S, Sitti M. 2006 Biologically inspired polymer microfibers with spatulate tips as repeatable fibrillar adhesives. *Appl. Phys. Lett.* **89**, 261911. (doi:10.1063/1.2424442)
- Liu J, Hui C-Y, Jagota A, Shen L. 2009 A model for static friction in a film-terminated microfibril array. *J. Appl. Phys.* **106**, 053520. (doi:10.1063/1.3211312)
- Shen L, Glassmaker N, Jagota A, Hui C-Y. 2008 Strongly enhanced static friction using a film-terminated fibrillar interface. *Soft Matter* **4**, 618. (doi:10.1039/b714737f)
- Shen L, Jagota A, Hui C-Y. 2009 Mechanism of sliding friction on a film-terminated fibrillar interface. *Langmuir* **25**, 2772–2780. (doi:10.1021/la803390x)
- Vajpayee S, Long R, Shen L, Jagota A, Hui C-Y. 2009 Effect of rate on adhesion and static friction of a film-terminated fibrillar interface. *Langmuir* **25**, 2765–2771. (doi:10.1021/la8033885)
- Varenberg M, Gorb S. 2007 Shearing of fibrillar adhesive microstructure: friction and shear-related changes in pull-off force. *J. R. Soc. Interface* **4**, 721–725. (doi:10.1098/rsif.2007.0222)
- Kim S, Aksak B, Sitti M. 2007 Enhanced friction of elastomer microfiber adhesives with spatulate tips. *Appl. Phys. Lett.* **91**, 221913. (doi:10.1063/1.2820755)
- Kumar A, Hui C-Y. 2011 Numerical study of shearing of a microfibre during friction testing of a microfibre array. *Proc. R. Soc. A* **467**, 1372–1389. (doi:10.1098/rspa.2010.0449)
- Nademann N, Kumar A, Goyal S, Hui C-Y. 2010 Buckling of sheared and compressed microfibrils. *J. R. Soc. Interface* **7**, 1581–1589. (doi:10.1098/rsif.2010.0147)
- Murphy M, Aksak B, Sitti M. 2007 Adhesion and anisotropic friction enhancements of angled heterogeneous micro-fiber arrays with spherical and spatula tips. *J. Adhes. Sci. Technol.* **21**, 1281–1296. (doi:10.1163/156856107782328380)
- Spuskanyuk A, Deshpande R, Arzt V. 2008 The effect of shape on the adhesion of fibrillar surfaces. *Acta Biomater.* **4**, 1669–1676. (doi:10.1016/j.actbio.2008.05.026)
- Gacoin E, Fretigny C, Chateauinois A. 2006 Measurement of the mechanical properties of thin films mechanically confined within contacts. *Tribol. Lett.* **21**, 245–252. (doi:10.1007/s11249-006-9030-y)
- Landau L, Lifshitz E. 1986 *Theory of elasticity*, 3rd edn. Oxford, UK: Butterworth Heinemann.
- Paretkar D, Bartlett M, McMeeking R, Crosby A, Arzt E. 2013 Buckling of an adhesive polymeric micropillar. *J. Adhes.* **89**, 140–158. (doi:10.1080/00218464.2013.731941)
- Barquins M. 1984 On a new mechanism in rubber friction. *Wear* **97**, 111–114. (doi:10.1016/0043-1648(84)90086-3)
- Sosson F, Chateauinois A, Creton C. 2005 Investigation of shear failure mechanisms of pressure-sensitive adhesives. *J. Polymer Sci. Part B* **43**, 3316–3330. (doi:10.1002/polb.20619)
- Abumsonwan U, Sitti M. 2012 Effect of retraction speed on adhesion of elastomer fibrillar structures. *Appl. Phys. Lett.* **101**, 211907. (doi:10.1063/1.4767360)
- Basire C, Fretigny C. 1999 Determination of viscoelastic moduli at a submicrometric scale. *Eur. Phys. J. Appl. Phys.* **6**, 323–329. (doi:10.1051/epjap:1999190)
- Ferry J. 1980 *Viscoelastic properties of polymers*, 3rd edn. London, UK: Wiley.
- Gravish N *et al.* 2010 Rate-dependent frictional adhesion in natural and synthetic gecko setae. *J. R. Soc. Interface* **7**, 259–269. (doi:10.1098/rsif.2009.0133)
- Kim S *et al.* 2010 Microstructured elastomeric surfaces with reversible adhesion for applications in assembly by transfer printing. *Proc. Natl Acad. Sci. USA* **107**, 2117.
- Menguc Y, Yang SY, Kim S, Rogers JA, Sitti M. 2012 Gecko-inspired controllable adhesive structures applied to micromanipulation. *Adv. Funct. Mater.* **22**, 1246–1254. (doi:10.1002/adfm.201101783)